Development, Implementation, and Assessment of a Continuum Model of Anisotropic Behavior of Polycrystalline Materials Due to Texture using a Second Order Structure Tensor

Brandon C. Templin

Center for Advanced Vehicular Systems
Mississippi State University, Mississippi State, MS 39762

Adetokunbo A. Adedoyin

Los Alamos National Laboratory, P.O. Box 1663, Los Alamos, NM 87545

Koffi Enakoutsa

Department of Mathematics, California State University Northridge
18111 Nordhoff Street, CA 91330
Department of Mathematics, University of California Los Angeles
520 Portola Plaza, Los Angeles, CA 90095

Douglas J. Bammann

Center for Advanced Vehicular Systems
Mississippi State University, Mississippi State, Mississippi 39762

Abstract

An Evolving Micro-structural Model of Inelasticicty is modified to capture evolving anisotropy resulting from underlying texture. Anisotropy is modeled via a second order orientation tensor resulting from the truncation to second order of an orientation distribution function and the temporal evolution of the tensor arises naturally from the closure properties associated with the truncation. A scalar variable defined by the Euclidean norm of the current state of the structure tensor and the direction of the rate of continuing plastic deformation, is incorporated in the flow rule. The model predictions is compared with yield surface data after various preloads for Aluminum 1100-O, differences in compression versus torsion for 304L SS and large directional changes in load path for AL 1100-O. Additional assessments of the model which compared the predictions of the model with and without textural effects are provided.

Keywords: Texture, Anisotropic Plasticity, Structure Tensor, Orientation Distribution Functions, Constitutive Model

1. Introduction

Material models are powerful tools commonly employed in areas not limited to the design of physical components and material processing. Specifically, material models capable of predicting evolving anisotropy are useful in the fabrication of parts that entails load path changes or directionally dependent material design. Inclusion of anisotropy in material models has been demonstrated using several modeling techniques that employ either orientation distribution functions [1, 2], crystal plasticity [3, 4, 5, 6, 7, 8, 9, 10], anisotropic yield criterion [11, 12, 13, 14, 15, 16, 17, 18, 19], or internal state variables (ISV) [20, 21, 22]. A material's yield behavior can be described adequately using a yield surface; a surface in stress space that describes the stress at which the material begins to plastically deform. If a material exhibits no directional dependence with respect to yield then its yield surface is isotropic. The evolution of an isotropic yield surface can be described by the symmetric expansion and translation of the yield surface using an isotropic and kinematic hardening respectively. Experimental observations of polycrystalline materials indicated that the yield behavior is directionally dependent at the onset of plastic deformation.

Anisotropic yield surfaces were captured in the experimental observations of Stout et al. [23] and Brown [24], in which the yield surface of a material was experimentally measured after various pre-loads using a five micro-strain offset definition of yield. They both observe a change in the shape and orientation of the yield surface. In addition to using isotropic and kinematic hardening state variables to describe the evolution of an anisotropic yield surface, the change in shape and rotation can be described by using distortion and rotational hardening respectively. Wegener and Schlegel [25] characterize this anisotropic behavior as a flattening, sharpening, symmetric shrinking, and symmetric expansion of the yield surface with respect to the direction of plastic deformation. Lopes et al. [26] observed distortion hardening in the uniaxial and shear testing of rolled Aluminum sheets. They also observed rotational hardening, as the material exhibited different yield behavior depending on the orientation of the specimen with respect to the rolling direction.

The development and evolution of anisotropy is physically linked to a phenomenon occurring within a material's micro-structure such as the changes in grain and sub-grain orientation and the concentration of dislocation entanglements within grain and sub-grain boundaries. Dafalias [27] demonstrated that anisotropic material behavior is a result of the cumulative effect of loading a polycrystalline material where its grains shared the same orientation to the direction of loading. Hockett et al. [28] attributed the differences in saturation stress of an Aluminum 1100 specimen loaded in multi-axial compression to the development of a stable sub-structures. Several specimens placed under multi-axial loading were found to reach a stable grain and sub-grain concentration with negligible dislocation entanglements within its grain and sub-grain boundaries while specimen under uniaxial loading never achieved stable grain concentrations and dislocation entanglements were still present within grain boundaries up to total compression strains of $3.2\,[in/in]$. This is in agreement with the findings of Wilsdorf and Hansen [29].

Commonly used yield criterion to account for material anisotropy are the Bishop-Hill [11, 12] and $Yld91$ [13, 14, 15] criterion. The Bishop-Hill criterion is a modified form of the Von Mises yield criterion using multiple scalar constants to account for material anisotropy while the yield criterion is based on the linear transformation of the deviatoric stress tensor described by a Hershey type yield criterion. Adebarro et al. [30, 31, 32] incorporated temperature dependence into the anisotropic parameters of the $Yld96$ yield criterion by fitting the parameters taken at multiple temperatures to 3^{rd} and 5^{th} order polynomials. Aretz [33] introduced deformation dependence to the anisotropic terms of the $Yld2003$ yield criterion by linear interpolation of the parameters taken at four finite strains. Stoughton and Woon [34] introduced a strain dependence into the anisotropic parameters by replacing the four flow stress terms used to determine the parameters with stress-strain relations. Desmorat and Roxane [35] proposed a non-quadratic plasticity criteria based on Kelvin modes to model with success the anisotropy in FCC nickel-base single crystals. Khan et al. [36] used extensive experimental results to develop a yield criterion to describe the anisotropic yield behavior and tension compression asymmetry characteristics of an electron beam single melt Ti6Al4V alloy and obtained good agreements between the experiments and their model predictions. Khan and Haowen [37] proposed an uncoupled anisotropic deformation and ductile fracture criterion for Ti6Al4V alloy; to effectively account for anisotropy and tension compression asymmetry in the material, a modified Hill anisotropic function proposed by the same authors is used to describe the geometry of the anisotropic fracture loci in principal stress space. Ku [38] used the Khan-Liu model to represent texture-induced anisotropy in AA7056 materials at different strain rates and temperatures. Qian and Wu [39] developed an analytic method to describe the evolution of asymmetric yield surface and assessed the accuracy of the method by applying it to several materials. Nixon et al. [40] developed an anisotropic elastic/plastic model to describe the quasi-static macroscopic response of α-titanium polycrystalline under quasi-static conditions at room temperature; their formulation includes (i) an anisotropic yield criterion that can capture strength-differential effects and (ii) an anisotropic hardening rule that accounts for texture evolution associated to twinning.

Evolving anisotropy has been modeled using a scalar coaxiality term that describes the alignment between the kinematic hardening and the direction of plastic flow. A variable of this type was first introduced in a tensorial hardening variable by Key and Krieg [41] in an effort to capture the shape of the uniaxial tensile stress in a load reversal test. Miller et al. [42] introduced a kinematic hardening evolution equation with an exponential dependence on a similar coaxiality term in an effort to replicate the rapid evolution of the flow stress in sudden load path changes of OFHC specimens with various amounts of rolling reduction. Wegener and Schelegel [25] suggested a kinematic hardening evolution equation that dependents on a coaxiality term to maximize the effect of hardening for a given change of plastic strain. Francois [43] suggested a model that can capture a hyper-egg yield surface by incorporating a parameter computed from the angle between the distorted stress and back-stress which allowed for a description of all possible states with a reduced set of variables. Shutov and Ihlemann [44] proposed a model with improved control of distortion hardening through the inclusion of a backstress-like second order distortion stress in which the yield criterion is dependent on the angle between the effective stress and the distortion stress. Bammann et al. [45] introduced the dependence of the isotropic hardening on a similar coaxiality term in order to account for the reduction in saturation stress of a specimen experiencing cyclic loading. Chaboche [46] discussed a similar coupling of isotropic and kinematic hardening to account for cyclic hardening and softening. Modeling of material anisotropy with the coaxiality term introduced by Key and Krieg [41] suggested the direction of anisotropy is entirely dependent on the kinematic hardening, however it was suggested by Feigenbaum and Dafalias [47] and [48] that the physics supports a distortion hardening that is independent of kinematic hardening. Prantil et al. [20] presented a method of evolving material anisotropy using a second order orientation tensor defined by the orientation distribution function of a unit vector bisecting two slip systems in double planar slip. Modeling evolving anisotropy in this manner allows the direction of anisotropy to evolve independently of the direction of kinematic hardening. Rogueiro et al. [22] introduced an anisotropic yield criterion using a coaxiality term that is dependent on the coaxiality of an orientation tensor describing anisotropy and the direction of plastic flow.

The method in which anisotropy is included into a material model can greatly affect the computational efficiency, accuracy, or complexity of the model. The ideal method of including anisotropy into any existing model would be in a manner that does not severely degrade or hinder the performance of the model while additionally not introducing a great deal of complexity to the model equations. Following these guidelines will allow for anisotropy to be easily implemented into a commercially available finite element software. One method for representing evolving anisotropy is a second order tensorial variable that evolves with plastic deformation. This representation accounts for anisotropy independent of other microstructural mechanisms. Anisotropic effects can then be easily included in the model equations through a scalar variable describing the angle between the developing texture and the direction of plastic deformation.

In this paper evolving anisotropy is modeled using a modified version of the Evolving Micro-structural Model of Inelasticity (EMMI) presented by Marin et al. [49]. Material anisotropy is modeled using a second order orientation tensor and incorporated into the flow rule via a scalar variable describing the coaxiality between the second order orientation tensor and the direction of plastic deformation. The representation of material anisotropy using a second order orientation tensor allows for the evolution of anisotropy independently of the kinematic hardening. The model is then tested against anisotropic yield data of Aluminum 1100-O presented by Brown [24]. In addition, incompabilities due to the presence of dislocation and disclination defects are also introduced in the model as the *curl* and the *curl* of the *curl* of the inelastic velocity gradient, and the distributions of the two defects are explored for several classical micromechanical problems. The rest of the paper is structured as follows.

- The first section describes the original EMMI model constitutive relations and its extended version to account for anisotropic and texture effects using structure tensor as described above.

- The section that follows compares the analytical yield surface the modified EMMI model predicts with the experimental results of Brown [24] for several sets of the model parameters. Besides theses comparisons, the section presents the texture effects predictive capabilities of the model for simple and complex loads.

The following mathematical operations in direct notation are used in the remainder of this paper. All bold face Greek or alphabetical letters indicate a tensorial quantity. Therefore given the following second rank tensorial quantities $\mathbf{A}$, $\mathbf{B}$, $\mathbf{C}$ and scalar variable γ, the norm of tensorial quantity is equivalent to $\|\mathbf{A}\| = [\mathbf{A} : \mathbf{A}]^{\frac{1}{2}}$ where the colon indicates a double contraction. The trace of a tensorial quantity is equivalent to $\mathrm{Tr}\,[\mathbf{A}] = \mathbf{A} : \mathbf{I}$. The deviatoric portion of a tensorial quantity is equivalent to $\acute{\mathbf{A}} = \mathbf{A} - \frac{1}{3}\mathrm{Tr}\,[\mathbf{A}]\,\mathbf{I}$. The product of two second rank tensorial quantities is equivalent $\mathbf{AB} = \mathbf{C}$. Associativity and distributivity with respect to γ in conjunction with the tensorial quantities $\mathbf{A}$, $\mathbf{B}$ and $\mathbf{C}$ hold for cases where scalar or vector sums are valid mathematical operations.

2. Methodology

2.1. The Constitutive equations of the anisotropic EMMI model

The model used in this study is the Evolving Micro-structural Model of Inelasticity (EMMI) outlined in Marin et al. [49] modified to accommodate material anisotropy. The EMMI model is a temperature and rate dependent phenomenological model that uses two internal state variables to capture material hardening. The constitutive equations of the EMMI model consist of the following elements.

2.1.1. Kinematics

The EMMI model equations are derived in the intermediate configuration stemming from the multiplicative split of the deformation gradient as presented by Lee and Liu [50] and Lee [51]. The deformation gradient is given by:

$$\mathbf{F} = \mathbf{F}_\mathrm{e}\mathbf{F}_\mathrm{p} \tag{1}$$

where $\mathbf{F}_\mathrm{p}$ is the plastic part of the total deformation gradient that facilitates mapping relevant variables from the reference material configuration to the intermediate. Similarly, $\mathbf{F}_\mathrm{e}$ is the elastic part of the total deformation gradient that aids in mapping relevant variables from the intermediate configuration to the current. The intermediate configuration is a load free configuration associated with permanent deformation due to internal defects while the current configuration represents a material configuration with an applied load. Following the thermodynamics for materials with internal state variables presented by Coleman and Noll [52] and Coleman and Gurtin [53], the model equations are derived in a compatible load free intermediate configuration and then pushed forward to the current configuration. The velocity gradient determined using Eq.(1) is:

$$\mathbf{l} = \dot{\mathbf{F}}\mathbf{F}^{-1}. \tag{2}$$

Therefore, the symmetric and an antisymmetric portions of the velocity gradient are:

$$\mathbf{d} = \frac{1}{2}\left[\mathbf{l} + \mathbf{l}^{\mathrm{T}}\right], \qquad \mathbf{w} = \frac{1}{2}\left[\mathbf{l} - \mathbf{l}^{\mathrm{T}}\right]. \tag{3}$$

Both portions of the velocity gradient can further be decomposed into an elastic and plastic parts such that:

$$\mathbf{d} = \mathbf{d}_{\mathrm{e}} + \mathbf{d}_{\mathrm{p}}, \qquad \mathbf{w} = \mathbf{w}_{\mathrm{e}} + \mathbf{w}_{\mathrm{p}}. \tag{4}$$

2.1.2. Evolution equations for the internal state variables

Assuming linear elasticity and a homogeneous isotropic material the Cauchy stress rate is:

$$\overset{\circ}{\boldsymbol{\sigma}} = \dot{\boldsymbol{\sigma}} - \mathbf{w}_{\mathrm{e}}\boldsymbol{\sigma} + \boldsymbol{\sigma}\mathbf{w}_{\mathrm{e}} = \frac{\boldsymbol{\sigma}}{\mu(\theta)}\frac{\partial \mu(\theta)}{\partial \theta}\dot{\theta} + 2\mu(\theta)\,\acute{\mathbf{d}}_{\mathrm{e}} + B(\theta)\,\mathrm{Tr}(\mathbf{d}_{\mathrm{e}})\mathbf{I} \tag{5}$$

where $\mu(\theta)$ is the temperature dependent shear modulus, $B(\theta)$ is the temperature dependent bulk modulus, and $\acute{\mathbf{d}}_{\mathrm{e}}$ is the deviatoric part of the symmetric portion of the velocity gradient determined by:

$$\acute{\mathbf{d}}_{\mathrm{e}} = \acute{\mathbf{d}} - \mathbf{d}_{\mathrm{p}}. \tag{6}$$

2.1.3. Isotropic hardening

The isotropic hardening internal state variable is associated with the annihilation and generation of statistically stored dislocations (SSD) where its evolution equation is cast in a hardening minus recovery format. The dynamic recovery portion was introduced by Kocks and Mecking [54] and Esterin and Mecking [55], while the static recovery portion was presented by Nes [56]. The evolution equation is given by:

$$\dot{\kappa} = \frac{\kappa}{\mu(\theta)}\frac{\partial \mu(\theta)}{\partial \theta}\dot{\theta} + (\mathrm{H}_{\kappa} - \mathrm{R}_{\mathrm{d}}\kappa)\,\dot{\bar{\epsilon}}_{\mathrm{p}} - \mathrm{R}_{\mathrm{s}}\kappa\sinh\left(\frac{\mathrm{Q}_{\mathrm{s}}}{2\mu \mathrm{C}_{\kappa}}\kappa\right) \tag{7}$$

where $\mathrm{R}_{\mathrm{d}}(\theta)$ is the dynamic recovery parameter, $\mathrm{R}_{\mathrm{s}}(\theta)$ is the static recovery parameter, and Q_{s} determines the order of the static recovery. The isotropic hardening modulus (H_{κ}) is reduced to a single variable given by:

$$\mathrm{H}_{\kappa} = 2\mu(\theta)\,\mathrm{C}_{\kappa}\mathrm{H} \tag{8}$$

2.1.4. Kinematic hardening

The back-stress is a stress-like internal state variable associated with the annihilation and generation of geometrically necessary dislocation (GND). In a similar approach, the evolution equation for the back-stress is cast in a hardening minus recovery format given by the equation

$$\overset{\circ}{\boldsymbol{\alpha}} = \dot{\boldsymbol{\alpha}} - \mathbf{w}_{\mathrm{e}}\boldsymbol{\alpha} + \boldsymbol{\alpha}\mathbf{w}_{\mathrm{e}} = \frac{\boldsymbol{\alpha}}{\mu(\theta)}\frac{\partial \mu(\theta)}{\partial \theta}\dot{\theta} + \mathrm{h}_{\alpha}\mathbf{d}_{\mathrm{p}} - \mathrm{r}_{\mathrm{d}}\dot{\bar{\epsilon}}^{\mathrm{p}}\sqrt{\frac{2}{3}}\,\|\boldsymbol{\alpha}\|\,\boldsymbol{\alpha} \tag{9}$$

where $\mathrm{r}_{\mathrm{d}}(\theta)$ is the recovery parameter and h_{α} is the kinematic hardening modulus which is reduced to a single variable

$$\mathrm{h}_{\alpha} = 2\mu(\theta)\,\mathrm{C}_{\alpha}\mathrm{h} \tag{10}$$

for simplicity.

2.1.5. Plastic flow

The plastic flow rule is given by:

$$\dot{\epsilon}_p = f\left(\theta\right)\sinh\left[\frac{\sigma_{eq}}{\kappa + Y_0} - 1\right]^{m(\theta)} \tag{11}$$

where θ is the temperature variable, $m\left(\theta\right)$ and $f\left(\theta\right)$ are temperature dependent constants associated with the rate sensitivity of the material, and Y_0 is the initial yield stress of the material. κ and $\boldsymbol{\alpha}$ are internal state variables associated with annihilation and generation of SSDs and GNDs, respectively. The equivalent stress is given by:

$$\sigma_{eq} = \sqrt{\frac{3}{2}\left\|\boldsymbol{\xi}\right\|} \tag{12}$$

where $\boldsymbol{\xi}$ is:

$$\boldsymbol{\xi} = \acute{\boldsymbol{\sigma}} - \frac{2}{3}\boldsymbol{\alpha} \tag{13}$$

and $\acute{\boldsymbol{\sigma}}$ is the deviatoric portion of the Cauchy stress.

2.2. Anisotropic flow rule

The evolution of anisotropy is represented by a second order orientation tensor outlined by Advani and Tucker [57, 58] and applied to polycrystalline materials by Prantil [20], in which the orientation tensor is defined by the ODF of a unit vector bisecting two active slip systems. The rate of change of material anisotropy is captured using the orientation tensor given by the equation:

$$\overset{\circ}{\mathbf{a}} = \dot{\mathbf{a}} - \mathbf{w}_{\mathrm{e}}\mathbf{a} + \mathbf{a}\mathbf{w}_{\mathrm{e}} = \lambda_{\mathrm{g}}\left(\mathbf{a}\mathbf{d}_{\mathrm{p}} + \mathbf{d}_{\mathrm{p}}\mathbf{a} + \frac{2}{3}\mathbf{d}_{\mathrm{p}}\right) + \frac{2}{3}\lambda_g\left(\mathbf{a} : \mathbf{d}_p\right)\mathbf{I} - 2\lambda_{\mathrm{g}}\left[\mathbf{B} : \mathbf{d}_{\mathrm{p}}\right] \tag{14}$$

where λ_{g} is a fitted parameter associated with the orientation of active slip systems and **B** is a fourth order orientation tensor defined as

$$B_{ijkl} = \oint F(\omega)\omega_i\omega_j\omega_k\omega_l d\omega \tag{15}$$

where where $F(\omega)$ is the orientation distribution function and ω is the unit vector bisecting two active slip systems. Details on the derivation of Eq.(14) are not easily accessible and for this reason only a summary of the process yielding to this equation is given here. A short presentation of the derivation of these equations is also provided in (Appendix A). This presentation is not indispensable but useful for a full grasp of the foundations of the model.

A closure approximation is required in order to reduce the fourth order orientation tensor to a function of the second order orientation tensor while maintaining all required symmetries of the higher order tensor. Linear and quadratic closure approximations are two commonly used closure approximations in which Advani and

Tucker [57, 58] showed that the linear closure approximation is exact for completely random orientations and the quadratic closure approximation is exact for highly aligned orientations. In order to maintain a higher degree of accuracy through all orientations, they recommend a hybrid closure approximation that is a linear combination of the linear and quadratic closure approximations using a scalar measure of orientation. The contraction operation $\mathbf{B} : \mathbf{d}_\mathrm{p}$ is given by:

$$\mathbf{B} : \mathbf{d}_\mathrm{p} = \frac{1}{7}\left[1 - \mathrm{f_a}\right]\left[(\mathbf{a} : \mathbf{d}_\mathrm{p})\mathbf{I} + 2\mathbf{a}\mathbf{d}_\mathrm{p} + 2\mathbf{d}_\mathrm{p}\mathbf{a}\right] + \frac{2}{35}\left[\mathrm{f_a} - 1\right]\mathbf{d}_\mathrm{p} + \mathrm{f_a}\left[\mathbf{a} : \mathbf{d}_\mathrm{p}\right]\mathbf{a} \quad (16)$$

where $\mathrm{f_a}$ is a scalar measure of orientation given by:

$$\mathrm{f_a} = \frac{3}{2}\mathbf{a} : \mathbf{a}^\mathrm{T} - \frac{1}{2}. \quad (17)$$

The evolving anisotropy is incorporated into the flow rule of the EMMI model through a scalar coaxiality term used to describe the degree of alignment between the direction of plastic flow and anisotropy and is given by:

$$\eta\left(\bar{\eta}\right) = \mathrm{C}_1 \cos\left(\bar{\eta}\right) + \mathrm{C}_2 \cos\left(2\bar{\eta}\right) + \mathrm{C}_3 \cos\left(3\bar{\eta}\right) + \mathrm{C}_4 \cos\left(4\bar{\eta}\right). \quad (18)$$

where C_1, C_2, C_3 and C_4 are fitted anisotropic parameters. The variable $\bar{\eta}$ is given by the equation:

$$\cos\left(\bar{\eta}\right) = \frac{\mathbf{a}}{\|\mathbf{a}\|} : \frac{\mathbf{d}_\mathrm{p}}{\|\mathbf{d}_\mathrm{p}\|} \quad (19)$$

where $\mathbf{a}$ is the orientation tensor. The form of the coaxiality term is extended from the work presented by Lubrada and Krajinovic [59] where they solved for the ODF equation by expanding the dot product of various damage orientation tensors with random direction tensors. This technique was later applied to polycrystalline materials by Rogueiro et al. [22]. Similar forms of ϕ were presented in the works of Wegener and Schlegel [25], Bammann et al. [45], Miller et al. [42], and Francois [43] where ϕ was defined using the direction of the back-stress and the plastic flow. The anisotropic parameters must sum up to unity, that is:

$$\sum_{\mathrm{n}=1}^{4} \mathrm{C_i} = 1; \quad (20)$$

this ensures that $\eta = 1$ when the direction of plastic flow is coaxial with the direction of developed anisotropy.

The symmetric portion of the velocity gradient is given by:

$$\mathbf{d}_\mathrm{p} = \sqrt{\frac{3}{2}}\dot{\epsilon}_\mathrm{p}\mathbf{N} \quad (21)$$

where $\mathbf{N}$ is the modified direction of plastic flow. The scalar quantity $\dot{\bar{\epsilon}}_{\mathrm{p}}$ is the equivalent plastic strain rate modified to account for the anisotropic behavior [22] which is defined as:

$$\dot{\bar{\epsilon}}_{\mathrm{p}} = \mathrm{f}\left(\theta\right)\sinh\left[\frac{\sigma_{\mathrm{eq}}}{\eta\left(\bar{\eta}\right)\kappa + \mathrm{Y}_{0}} - 1\right]^{\mathrm{m}(\theta)} \tag{22}$$

where $m\left(\theta\right)$ and $f\left(\theta\right)$ are constants associated with the rate sensitivity of the material. $\eta\left(\bar{\eta}\right)$ is the scalar coaxiality term and Y_0 is the initial yield stress of the material. The variables κ and $\boldsymbol{\alpha}$ are internal state variables associated with annihilation and generation of SSDs and GNDs, respectively. The equivalent stress is given by:

$$\sigma_{eq} = \sqrt{\frac{3}{2}}\left\|\boldsymbol{\xi}\right\| \tag{23}$$

where $\boldsymbol{\xi}$ is:

$$\boldsymbol{\xi} = \acute{\boldsymbol{\sigma}} - \frac{2}{3}\boldsymbol{\alpha} \tag{24}$$

and $\acute{\boldsymbol{\sigma}}$ is the deviatoric portion of the Cauchy stress.

The modified direction of plastic flow must account for the directional effects of material anisotropy and is therefore given by:

$$\mathbf{N} = \frac{\mathbf{n}_{\mathrm{T}}}{\left\|\mathbf{n}_{\mathrm{T}}\right\|} \tag{25}$$

where $\mathbf{n}_{\mathrm{T}}$ is defined as:

$$\mathbf{n}_{\mathrm{T}} = \mathbf{n}_{\boldsymbol{\sigma}} - \mathrm{C}_{\boldsymbol{\sigma}\eta}\mathbf{n}_{\mathrm{A}} \tag{26}$$

where $\mathbf{n}_{\boldsymbol{\sigma}}$ is the direction of the equivalent stress given by:

$$\mathbf{n}_{\boldsymbol{\sigma}} = \frac{\boldsymbol{\xi}}{\left\|\boldsymbol{\xi}\right\|}. \tag{27}$$

The scalar $\mathrm{C}_{\boldsymbol{\sigma}\eta}$ is the ratio:

$$\mathrm{C}_{\boldsymbol{\sigma}\eta} = \frac{\sigma_{eq}}{\eta\left(\bar{\eta}\right)}. \tag{28}$$

Details on the derivation of Eqs.(25, 26, 27, 28) and the ensuing equations Eqs.(29, 30, 31, 32, 33) are provided in Appendix A and Appendix B.

The direction of plastic flow imposed by the anisotropic term $\mathbf{n}_{\mathbf{A}}$ is defined by:

$$\mathbf{n}_{\mathrm{A}} = \zeta\left(\bar{\eta}\right)\left(\mathbf{a} - \mathrm{C}_{\xi\mathbf{a}}\frac{\boldsymbol{\xi}}{\left\|\boldsymbol{\xi}\right\|}\right) \tag{29}$$

where the scalar $\zeta(\bar{\eta})$ is given by the expression

$$\begin{aligned}\zeta(\bar{\eta}) &= \mathrm{m}\left[\mathrm{C}_1 + 4\mathrm{C}_2\cos(\bar{\eta}) + 3\mathrm{C}_3\left(4\cos^2(\bar{\eta}) - 1\right)\right] \\ &+ \mathrm{m}\left[16\mathrm{C}_4\cos(\bar{\eta})\left(2\cos^2(\bar{\eta}) - 1\right)\right]\end{aligned} \tag{30}$$

where m is difined as

$$\mathrm{m} = \left[\|\xi\|\,\|\mathbf{a}\|\right]^{-1}. \tag{31}$$

The scalar $\mathrm{C}_{\xi,\mathbf{a}}$ is given by:

$$\mathrm{C}_{\xi,\mathbf{a}} = \frac{\boldsymbol{\xi} : \mathbf{a}}{\|\boldsymbol{\xi}\|}. \tag{32}$$

The plastic part of the skew symmetric portion of the velocity gradient follows from a constitutive definition presented by Prantil [20] and is given by the expression

$$\mathbf{w}^{\mathrm{p}} = \frac{1}{\lambda_{\mathrm{g}}}\left(\mathbf{a}\mathbf{d}_{\mathrm{p}} - \mathbf{d}_{\mathrm{p}}\mathbf{a}\right) \tag{33}$$

where λ_g is a fitted constant associated with the angle between active slip systems. Bammann and Aifantis [60] proposed a similar form of the plastic spin based on the micromechanics of single slip. Other forms were proposed by Dafalias [61] and Loret [62] using representation theorem.

3. Results/Discussion

In this section model predictions will be compared to the small strain offset yield surface data of Brown [24], in which yield is determined by probing stress space after various preloads. The precise steps employed by Brown were included in the simulations. After a prestrain, loading was simulated, from the new prestrain origin, in a direction in stress space until the 0.005 strain offset was reached. Then the material is unloaded back to the origin, followed by repetition of the process in a new direction. An alternate approach would be to ignore the effect of loading and unloading, and determing the parameters that give the best ”fit” to the experimentally observed yiled surface. The two approaches result in different sets of parameters and in matching the exact steps used in the experimental process. The model is simplified following the assumption that temperature change in the material is negligible henceforth all thermally varying components are zero and the material remains at the initial temperature. In addition, we assume material anisotropy occurs in the direction of plastic deformation; therefore the coaxiality term remains at unity ($\eta = 1.0$). This also implies that an isotropic material loaded uniaxially will not exhibit any anisotropy in any other direction. Based on these assumptions, an uniaxial stress-strain data is sufficient for identifying the parameters associated with the plastic part of the symmetric portion of the velocity gradient $\mathbf{d}_p$. This also hold true for the isotropic ($\dot{\kappa}$) and kinematic ($\dot{\boldsymbol{\alpha}}$) hardening rates. The model is further simplified following the assumption that the static recovery contribution to the isotropic hardening rate is negligible ($R_s = 0$).

Parameter	Symbol	Value	Unit
$\dot{\kappa}$-Equation			
Hardening	H_{κ}	11850	psi
Recovery	R_d	2.26	-
Recovery	R_s	0	1/s
Parameter	Q_s	1	-
Parameter	C_s	1	-
$\dot{\boldsymbol{\alpha}}$-Equation			
Hardening	$h_{\boldsymbol{\alpha}}$	1.24E6	psi
Recovery	r_d	0.0245	-
Parameter	C_a	1	-
$\dot{a}$-Equation			
Parameter	C_1	2	-
Parameter	C_2	4	-
Parameter	C_3	2	-
Parameter	C_4	1	-
Parameter	λ_g	1.3E5	-
$\dot{\boldsymbol{\sigma}}$-Equation			
Yield Stress	Y_0	1700	psi
Shear Modulus	μ	3.6E6	psi
Elastic Modulus	E	10E6	psi
Poisson's Ratio	ν	0.3	-

Table 1: Material parameters for Aluminum 1100-O determined using multiple strain rate experimental data of Hockett [63] and Brown [24]. Anisotropic parameters were fitted to anisotropic data of specimen 06 in Brown [24]. The yield, shear, and elastic modulus are those reported in Brown [24].

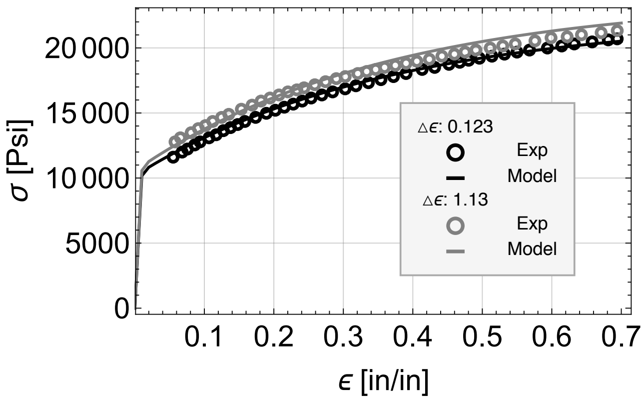

Figure 1: EMMI model parameters to fit to uniaxial compression data of Aluminum 1100-O [63]

From stability analysis of differential equations the efficient approach to integrating any system(s) of ordinary equations is an implicit time marching algorithm. An implicit time marching approach is efficient because larger time steps (Δt) can be taken without compromising the numerical solution. The EMMI model equations are modified here to account for texture and anisotropy requires additional numerical considerations.

Numerical integration was performed using a material point simulator written in Mathematica 9 initially designed by [64, 65] to model multiphase materials. Without any consideration for texture and anisotropy, the flow rule can be evaluated by treating the effective plastic flow as either a function to be computed at every time step or as an additional evolution equation. With η incorporated into the net effective plastic flow there is an additional dependence on the plastic part of the symmetric portion of the velocity gradient which is directly dependent on the effective plastic flow, that is, the equation

$$\eta(\phi) = \hat{f}(\dot{\bar{\epsilon}}_{\mathrm{p}}) \tag{34}$$

where $\hat{f}$ implies a functional. Therefore, the initial conditions for both plastic strain (ϵ_p) and plastic strain rate ($\dot{\epsilon}_p$) have to be prescribed. This numerical caveats becomes important when implementing an either implicit or explicit integration algorithm for a material subroutine in ABAQUS [66] finite element code.

The initial yield stress was assumed to be the approximate stress that demonstrated a deviation from linearity in the uniaxial testing presented in Brown [24]. The uniaxial parameters were simultaneously fitted to uniaxial compression data presented by Hockett [63] taken at constant compression strain rates of $\dot{\epsilon} = 0.123s^{-1}$ and $\dot{\epsilon} = 1.13s^{-1}$ at room temperature and the small strain uniaxial data presented by Brown [24].

The uniaxial stress strain data presented by Hockett was performed via cam plastometer tests providing a constant axial compression deformation rate. Figure 1 is a

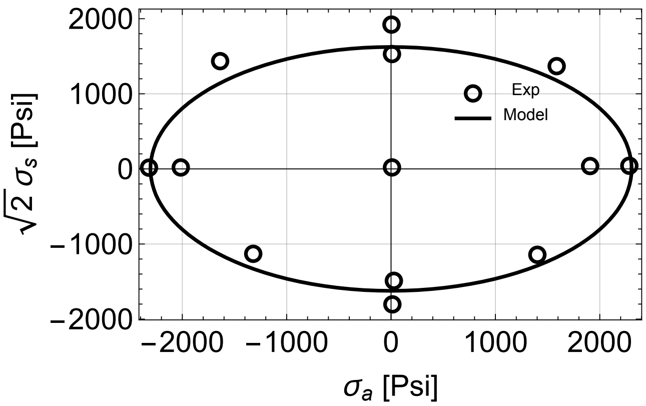

Figure 2: Initial isotropic yield surface of Aluminum 1100-O predicted by EMMI model and compared to the isotropic yield surface experimentally obtained by Brown [24]

plot comparing the fitted uniaxial model with multiple constant strain rate data of Aluminum 1100-O presented by Hockett [63]. Table 1 is a table listing all of the fitted parameters and relevant material properties for the model. The subsequent anisotropic yield surfaces of specimen 06 obtained by Brown [24] were then used to determine the additional anisotropic parameters $\mathrm{C}_1, \mathrm{C}_2, \mathrm{C}_3, \mathrm{C}_4$ and λ_g to best capture the shape change and rotation of the yield surface. The initial isotropic yield surface of Aluminum 1100-O was determined by integrating equations 22, 7, 9 at a constant total stress rate of $\dot{\sigma}$ = 85 psi/min at 128 different evenly spaced loading directions in stress space. The initial conditions for each of the integrated equations were set to zero in determination of the isotropic yield surface. Figure 2 is a plot comparing the model prediction of the initial isotropic yield surface to the initial isotropic yield surface presented in Brown [24].

The first inelastic state was used to determine the anisotropic parameters $\mathrm{C}_1, \mathrm{C}_2, \mathrm{C}_3, \mathrm{C}_4$ which capture the shape change of the yield surface. The values of the internal state variables at the first preload point were determined by integrating equations 7, 9 and 22 in pure reverse shear to a preload state with the axial component $\sigma_\mathrm{a} = 0$ psi and shear component $\sqrt{2}\sigma_\mathrm{s} = -3353$ psi at a total constant stress rate of 85 psi/min. The initial conditions of the internal state variables were set to all values equal to 0 to replicate initial isotropic undeformed conditions. The internal state variables κ and α at the end of the load step were then stored for yield surface calculation. The structure tensor $\mathbf{a}$ is assumed to be fully evolved in the reverse shear direction, stemming from the assumption there was no existing anisotropy prior to the initial preload step.

The anisotropic yield surface for the first inelastic state was determined by integrating equations 22, 7, 9 from the experimentally obtained center of the yield surface at the first inelastic state, with $\sigma_\mathrm{a} = 0$ ksi, $\sigma_\mathrm{s} = -2400$ ksi the axial and shear components of the center of the yield surface respectively. The internal state variables from

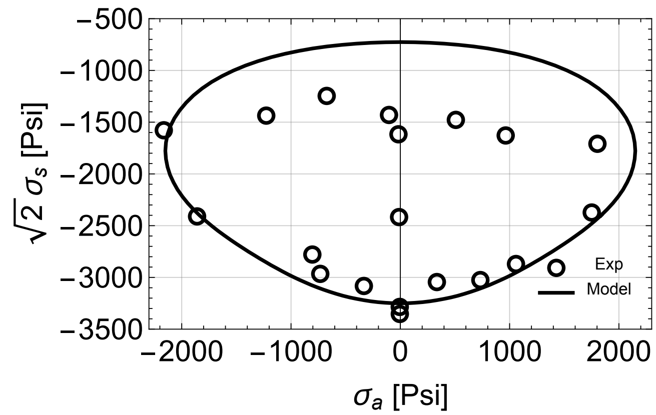

Figure 3: Comparison of experimentally obtained anisotropic yield surface of Aluminum 1100-O by Brown [24] to the anisotropic yield surface predicted by the model. Inelastic state of Aluminum 1100-O at a preload defined by an axial stress component $\sigma_A = 0$ psi and shear stress component $\sqrt{2}\sigma_s = -542$ loaded from an initially isotropic unloaded state

the end of the first preload step are used as initial conditions for the respective evolution equations for integration from the center of the yield surface. To determine a yield point, equations 22, 7, 9 are then integrated in a specified load direction at a total stress rate of 85 psi/min until an accumulated equivalent plastic strain of 5 microstrain is achieved. The stress state at the prescribed offset is then stored as the yield stress and the process repeated for 128 evenly spaced load directions. Figure 3 is a plot comparing the predicted anisotropic yield surface from the model to the experimental data of the first inelastic state presented by Brown [24]. The model replicates the overall shape change of the yield surface quite well, characterized by the sharpening of the yield surface in the direction of the preload point and the flattening of the yield surface on the side opposite of the preload point. The model does slightly over-predict the curvature of the yield surface on the side opposite the preload point.

The state variables κ, $\boldsymbol{\alpha}$ and $\mathbf{a}$ at the second preload was determined by integrating equations 22, 14, 7, 9 from the first preload to the second preload defined by an axial and shear component of $\sigma_A = 508$ ksi, $\sigma_s = -3454$ ksi respectively, at a constant total stress rate of 85 psi/min. The final values at the first preload point of the internal state variables κ and α, the structure tensor $\mathbf{a}$, and the stress σ were used as the initial conditions of the respective evolution equations in the integration from the first preload point to the second preload point. The final state of κ, α, and $\mathbf{a}$ at the end of the second preload step were stored and used as initial conditions for the integration of equations 22, 7, 9 in determination of each yield point of the second inelastic state. The material is not being loaded from an initially isotropic condition, therefore the structure tensor $\mathbf{a}$ must be evolved with deformation from the first preload point to the second preload point, however it is assumed that the 5 microstrain in yield stress determination has little effect on the direction of anisotropy and the direction of anisotropy is held constant in the determination of the yield points in the yield surface determination. The anisotropic parameter λ_g is physically linked to the orientation of the active slip systems and controls the rate at which the structure tensor evolves towards the direction of deformation. The λ_g controls how rapidly the structure tensor reaches a steady state that is coaxial with the direction of plastic deformation.

The yield surface of the second inelastic state was determined in a similar manner as the yield surface of the first inelastic state: integrating equations 22, 7, 9 from the experimentally obtained center of the yield surface with axial and shear components $\sigma_a = 525$ ksi, $\sigma_s = -2500$ ksi respectively. The values of κ, $\boldsymbol{\alpha}$, and $\mathbf{a}$ at the end of the second preload step were used as initial conditions in the integration of equations 22, 7, 9 in the calculation of the yield stresses of the second inelastic state. Equations 22, 7, 9 were then integrated from the center of the yield surface in a prescribed stress direction with a total stress rate of 85 psi/min until an accumulated equivalent plastic strain of 5 microstrain was achieved and the stress at the 5 microstrain point was stored as the yield stress. The process was repeated for 128 evenly spaced load directions and the axial and shear components of the yield stresses plotted.

Figure 4 is a comparison of the experimental yield surface versus the yield surface predicted by the model of the second inelastic state. The experimental yield surface shows a rotation of the yield surface towards the direction of the preload accompanied with a slight elongation of the yield surface to an egg shape, while the flattened side of the yield surface remains relatively unchanged. The rate at which the yield surface rotates is proportional to the anisotropic term λ_g, which physically describes the rate the underlying material anisotropy develops in the respective direction of loading. The model is able to replicate the overall rotation and elongation of the yield surface quite well, but predicts a different curvature on the side of the yield surface opposite of the preload point. The state of the variables κ, $\boldsymbol{\alpha}$ and $\mathbf{a}$ at the third preload was determined by integrating equations 22, 14, 7, 9 from the second preload to the final preload having values for the axial and shear components $\sigma_a = 0$ ksi, $\sigma_s - 542$ ksi at a constant total stress rate of 85 psi/min. The values of κ, $\boldsymbol{\alpha}$ and $\mathbf{a}$ at the end of the second preload step were used as initial conditions for the integration of their respective evolution equations from the second preload point to the third preload point.

The yield surface for the third step was determined in a similar fashion as the yield surface for the first and second inelastic states using the experimentally obtained yield surface center with axial and shear components $\sigma_a = 0$ ksi $\sigma_s = -1300$ ksi respectively. The values of κ, $\boldsymbol{\alpha}$ and $\mathbf{a}$ from the end of the third preload step were used as the initial conditions at the center of the yield surface corresponding to the third inelastic state. Equations 22, 14, 7, 9 were then integrated at 128 evenly spaced loading directions at a total stress rate of 85 psi/min until an accumulative equivalent plastic strain of 5 microstrain was achieved. Figure 5 is a plot comparing the prediction of the third inelastic state to the experimentally obtained yield surface. The experimental yield surface depicted a flattening of both the side of the yield surface facing the preload point and the side opposite the preload point. The model predicts the flattening of the side opposite the preload point, but predicts a slight sharpening of the yield surface near the preload point. The sharpening predicted by the model indicates the texture is develop-

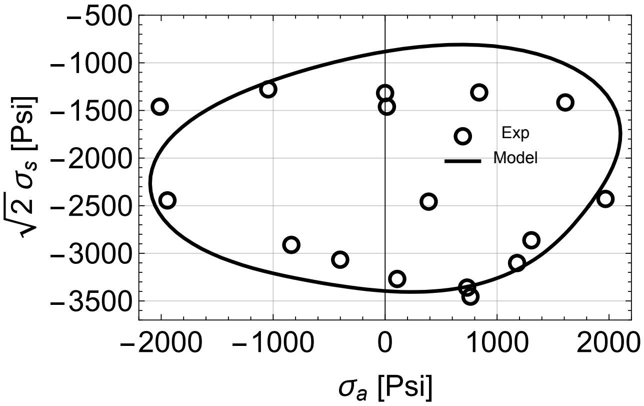

Figure 4: Comparison of experimentally obtained anisotropic yield surface of Aluminum 1100-O by Brown [24] to the anisotropic yield surface predicted by the model. Inelastic state of Aluminum 1100-O at a preload defined by an axial stress component $\sigma_A = 508$ psi and shear stress component $\sqrt{2}\sigma_s = -3454$ loaded from an initial preload defined by an axial stress component $\sigma_a = 0$ psi and shear stress component $\sqrt{2}\sigma_s = -3353$ psi

ing in the positive shear direction even though the load point is still in the reverse shear region of stress space.

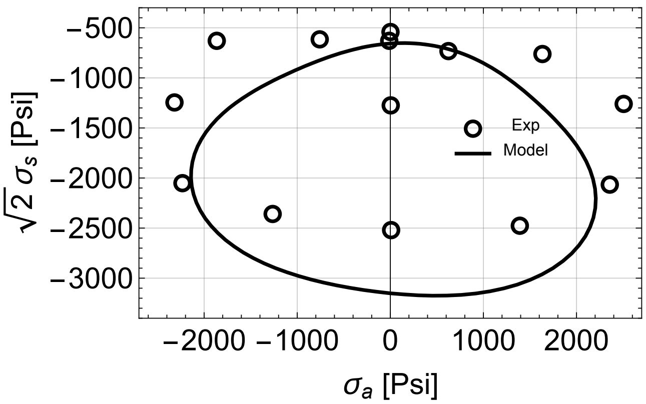

Figure 5: Comparison of experimentally obtained anisotropic yield surface of Aluminum 1100-O by Brown [24] to the anisotropic yield surface predicted by the model. Inelastic state of Aluminum 1100-O at a preload defined by an axial stress component $\sigma_A = 0$ psi and shear stress component $\sqrt{2}\sigma_s = -542$ loaded from an initial preload defined by an axial stress component $\sigma_A = 508$ psi and shear stress component $\sqrt{2}\sigma_s = -3454$ psi

4. Qualitative assessment of the model with texture effects

Accounting for textural evolution in a material model is important because a realistic material response is necessary for a more accurate prediction. In an effort to test the efficacy of the EMMI model with textural evolution we perform a multi-load numerical experiment where by we specify a piecewise and distinct loading condition in between a specified time interval.

The simulations were perfomred using [64, 65] numerical implementation of the model. In these simulations, we turn on and off the differential equation responsible for textural evolution Eq. 14. Conceptually, we start by simulating a rolling process. We then proceed by undoing some of the rolling and rapidly following that up with a shearing of the specimen. Herein, we believe that a model that accounts for textural evolution must capture the effects of the partial unrolling which creates a non-uniformly aligned material.

For Stage 1, we load the specimen in tension by specifying a positive magnitude for $l^1_{2,2} = 0.5/s$ component and therefore for volume preserving deformation we specify a negative magnitude on the $l^1_{1,1} = -0.25/s$ and $l^1_{3,3} = -0.25/s$ components. The index zero e.g. $l^0_{2,2}$ indicates $l_{2,2}$ for stage zero of the numerical experiment. For Stage 2, we load the specimen in compression with $l^2_{2,2} = -0.9/s$, and therefore for volume preserving deformation we specify a positive magnitude in the $l^2_{1,1} = 0.05/s$ and $l^2_{3,3} = 0.05/s$ components. For stage 3, we load the specimen in shear by specifying a $l^3_{1,2} = 0.6/s$ component of the velocity gradient.

To proceed, we integrate the constituve equations of the model while driving the deformation with the differential equation responsible for updating the state of the material

$$\dot{\mathbf{F}} = \mathbf{L}\mathbf{F}. \tag{35}$$

We replace the elastic symmetrical and anti-symmetrical portions (abbreviated by Sym and ASym, respectively) of the velocity gradient in the equations of interest with:

$$\mathbf{d}_e = \mathrm{Sym}\left(\dot{\mathbf{F}}\mathbf{F}^{-1}\right) - \mathbf{d}_p \quad \text{and} \quad \mathbf{w}_e = \mathrm{ASym}\left(\dot{\mathbf{F}}\mathbf{F}^{-1}\right) - \mathbf{w}_p \tag{36}$$

Figure 6 and 7 show the material response and corresponding plastic flow for all pertinent components of the deviatoric portion of the Cauchy stress tensor and flow rate tensor with and without accounting for textural evolution. As shown, intuitively we expect less plastic flow (fig. 7b) in transition region from Tension-Compression to Shear relative to the case where material texture is not accounted for. This is due to the mechanically induced non-uniform texture in the material. $dp_{1,1}$ (fig. 7a) of the plastic flow components shows an increased plastic flow in the aforementioned region and hence a corresponding increase material response. In addition, there is also less plastic flow in the $dp_{2,2}$ relative to the $dp_{1,1}$ as the non-uniformity was predominantly introduced in the $dp_{2,2}$ component of the velocity gradient.

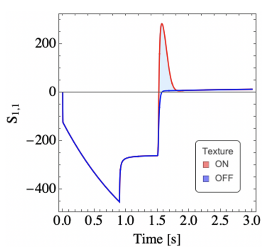

(a) Time history of σ_{11}.

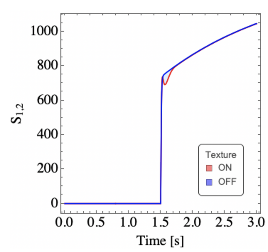

(b) Time history of σ_{12}.

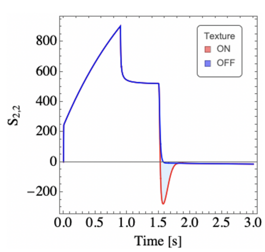

(c) Time history of σ_{22}.

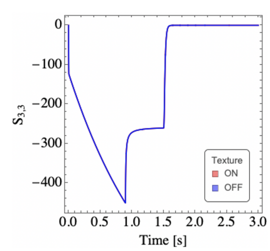

(d) Time history of σ_{33}.

Figure 6: Material response for the cases with and without textural effects. The load is a tension followed by a compression and shear. Significant component of the Cauchy stress tensor were presented.

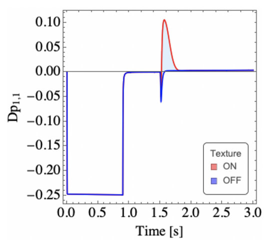

(a) Time history of $dp_{1,1}$

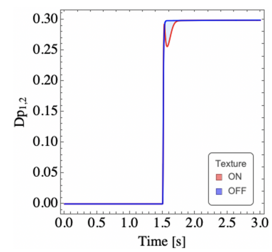

(b) Time history of $dp_{1,2}$

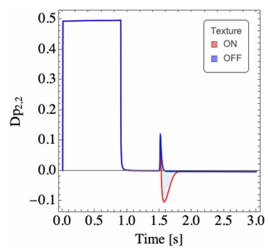

(c) Time history of $dp_{2,2}$

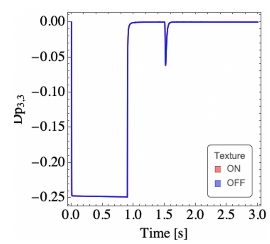

(d) Time history of $dp_{3,3}$

Figure 7: Flow rate histories for the cases with amd without textural effects. The load is a tension followed by a compression and shear. Significant components of the flow rate tensor are displayed.

5. Conclusion

The Evolving Micro-structural Model of Inelasticity, an existing rate and temperature dependent physically based plasticity model, was modified to account for evolving anisotropy. This is in addition to the normal anisotropy associated with kinematic hardening. Anisotropy was characterized by a second order orientation tensor, resulting from the truncation of the orientation distribution function associated with texture. A constitutive equation for the plastic spin (skew symmetric part of the plastic velocity gradient) has been derived in terms of this structure tensor. In addition, the structure tensor was incorporated into the flow rule of the EMMI model via a scalar variable describing the coaxiality of the structure tensor with the direction of the plastic rate deformation. This coaxiality term scales the isotropic hardening variable in the flow rule emulating the predicition from crystal plasticity that isotropic hardening (internal strength resisting plastic flow) is larger if the direction of plastic flow continues in the same (or nearly the same) direction of previous inelastic flow which is charaterized by the structure tensor (texture). This internal strength becomes smaller as the difference in direction between the plastic flow and the the structure tensor increases. The closure properties associated with the truncation of the ODF series to second order (Advani and Tucker [57]) yield a prescribed evolution equation for the second order structure tensor. These modifications to the model were compared with experimentally obtained anisotropic yield surfaces of Aluminum 1100-O by Brown [24]. The anisotropic parameters of the model were fitted to replicate the evolution of the first three anisotropic yield surfaces of specimen 06 presented by Brown. The predictions of the model compared favorably with the yield surfaces observed by Brown [24], predicting similar shape changes and rotations of the flow surfaces after various preloads. Finally, we compared the material response under several complex loading conditions for two cases: the case where the model accounts for textural effects and the case where it does not. The results demonstrate the ability of the model to capture complex history effects related to texture induced anisotropy.

6. Acknowledgment

The authors acknowledge the following institutions at Mississippi State University for their support of this work: (1.) Bagley College of Engineering (2.) The Department of Mechanical Engineering (3.) The Center for Advanced Vehicular Systems.

References

[1] M. Rashid, Texture evolution and plastic response of two-dimensional polycrystals, Journal of the Mechanics and Physics of Solids 40 (5) (1992) 1009–1029.

[2] J. Ning, E. Aifantis, Anisotropic yield and plastic flow of polycrystalline solids, International journal of plasticity 12 (10) (1996) 1221–1240.

[3] D. Peirce, R. Asaro, A. Needleman, An analysis of nonuniform and localized deformation in ductile single crystals, Acta metallurgica 30 (6) (1982) 1087–1119.

[4] R. Becker, J. Butler, H. Hu, L. Lalli, Analysis of an aluminum single crystal with unstable initial orientation (001)[110] in channel die compression, Metallurgical Transactions A 22 (1) (1991) 45–58.

[5] R. Becker, Analysis of texture evolution in channel die compression - i. effects of grain interaction, Acta metallurgica et materialia 39 (6) (1991) 1211–1230.

[6] F. Roters, P. Eisenlohr, L. Hantcherli, D. D. Tjahjanto, T. R. Bieler, D. Raabe, Overview of constitutive laws, kinematics, homogenization and multiscale methods in crystal plasticity finite-element modeling: Theory, experiments, applications, Acta Materialia 58 (4) (2010) 1152–1211.

[7] P. Van Houtte, J. Gawad, P. Eyckens, B. Van Bael, G. Samaey, D. Roose, A full-field strategy to take texture-induced anisotropy into account during fe simulations of metal forming processes, JOM Journal of the Minerals, Metals and Materials Society 63 (11) (2011) 37–43.

[8] D. Raabe, F. Roters, Using texture components in crystal plasticity finite element simulations, International Journal of Plasticity 20 (3) (2004) 339 – 361, owen Richmond Memorial Special Issue.

[9] L. Hu, S.-y. Jiang, Y.-q. Zhang, X.-m. Zhu, D. Sun, Texture evolution and inhomogeneous deformation of polycrystalline cu based on crystal plasticity finite element method and particle swarm optimization algorithm, Journal of Central South University 24 (12) (2017) 2747–2756.

[10] K. Min, W. Jeong, S. Hong, C. Lee, P.-R. Cha, H. Han, M.-G. Lee, Integrated crystal plasticity and phase field model for prediction of recrystallization texture and anisotropic mechanical properties of cold-rolled ultra-low carbon steels, International Journal of Plasticity 127 (2020) 102644.

[11] J. Bishop, R. Hill, Cxxviii. a theoretical derivation of the plastic properties of a polycrystalline face-centred metal, The London, Edinburgh, and Dublin Philosophical Magazine and Journal of Science 42 (334) (1951) 1298–1307.

[12] R. Hill, The elastic behaviour of a crystalline aggregate, Proceedings of the Physical Society. Section A 65 (5) (1952) 349.

[13] F. Barlat, J. W. Yoon, O. Cazacu, On linear transformations of stress tensors for the description of plastic anisotropy, International Journal of Plasticity 23 (5) (2007) 876–896.

[14] F. Barlat, H. Aretz, J. Yoon, M. Karabin, J. Brem, R. Dick, Linear transfomation-based anisotropic yield functions, International Journal of Plasticity 21 (5) (2005) 1009–1039.

[15] F. Barlat, J. Brem, J. Yoon, K. Chung, R. Dick, D. Lege, F. Pourboghrat, S.-H. Choi, E. Chu, Plane stress yield function for aluminum alloy sheets part 1: theory, International Journal of Plasticity 19 (9) (2003) 1297–1319.

[16] A. Taherizadeh, D. E. Green, J. W. Yoon, Evaluation of advanced anisotropic models with mixed hardening for general associated and non-associated flow metal plasticity, International Journal of Plasticity 27 (11) (2011) 1781–1802.

[17] T. Kuwabara, K. Hashimoto, E. Iizuka, J. W. Yoon, Effect of anisotropic yield functions on the accuracy of hole expansion simulations, Journal of Materials Processing Technology 211 (3) (2011) 475–481.

[18] F. Roters, Using texture components in crystal plasticity finite element simulations, International Journal of Plasticity 20 (2004) 339–361.

[19] P. P. Indurkar, S. Baweja, R. Perez, S. P. Joshi, Predicting textural variability effects in the anisotropic plasticity and stability of hexagonal metals: Application to magnesium and its alloys, International Journal of Plasticity 132 (2020) 102762.

[20] V. C. Prantil, J. T. Jenkins, P. R. Dawson, An analysis of texture and plastic spin for planar polycrystals, Journal of the Mechanics and Physics of Solids 41 (8) (1993) 1357–1382.

[21] V. C. Prantil, An analytical description of macroscopic anisotropy for planar polycrystalline aggregates, Cornell University, January, 1992.

[22] R. Regueiro, D. Bammann, E. Marin, K. Garikipati, A nonlocal phenomenological anisotropic finite deformation plasticity model accounting for dislocation defects, Transactions of the ASME: Journal of engineering materials and technology 124 (3) (2002) 380–386.

[23] M. Stout, P. Martin, D. Helling, G. Canova, Multiaxial yield behavior of 1100 aluminum following various magnitudes of prestrain, International Journal of Plasticity 1 (2) (1985) 163–174.

[24] A. A. Brown, An experimental study of the strain-space formulation of plasticity, University of California, Berkeley, 2000.

[25] K. Wegener, M. Schlegel, Suitability of yield functions for the approximation of subsequent yield surfaces, International Journal of Plasticity 12 (9) (1996) 1151–1177.

[26] A. Lopes, F. Barlat, J. Gracio, J. F. Duarte, E. Rauch, Effect of texture and microstructure on strain hardening anisotropy for aluminum deformed in uniaxial tension and simple shear, International Journal of Plasticity 19 (1) (2003) 1–22.

[27] Y. F. Dafalias, Orientation distribution function in non-affine rotations, Journal of the Mechanics and Physics of Solids 49 (11) (2001) 2493–2516.

[28] P. Armstrong, J. Hockett, O. Sherby, Large strain multidirectional deformation of 1100 aluminum at 300 k, Journal of the Mechanics and Physics of Solids 30 (1-2) (1982) 37–58.

[29] D. Kuhlmann-Wilsdorf, N. Hansen, Geometrically necessary, incidental and subgrain boundaries, Scripta metallurgica et materialia 25 (7) (1991) 1557–1562.

[30] N. Abedrabbo, F. Pourboghrat, J. Carsley, Forming of aluminum alloys at elevated temperatures–part 1: Material characterization, International Journal of plasticity 22 (2) (2006) 314–341.

[31] N. Abedrabbo, F. Pourboghrat, J. Carsley, Forming of aluminum alloys at elevated temperatures–part 2: Numerical modeling and experimental verification, International Journal of Plasticity 22 (2) (2006) 342–373.

[32] N. Abedrabbo, F. Pourboghrat, J. Carsley, Forming of aa5182-o and aa5754-o at elevated temperatures using coupled thermo-mechanical finite element models, International Journal of Plasticity 23 (5) (2007) 841–875.

[33] H. Aretz, A simple isotropic-distortional hardening model and its application in elastic–plastic analysis of localized necking in orthotropic sheet metals, International Journal of Plasticity 24 (9) (2008) 1457–1480.

[34] T. B. Stoughton, J. W. Yoon, Anisotropic hardening and non-associated flow in proportional loading of sheet metals, International Journal of Plasticity 25 (9) (2009) 1777–1817.

[35] R. Desmorat, R. Marull, Non-quadratic kelvin modes based plasticity criteria for anisotropic materials, International Journal of Plasticity 27 (3) (2011) 328–351.

[36] A. S. Khan, S. Yu, H. Liu, Deformation induced anisotropic responses of ti6al4v alloy part ii: A strain rate and temperature dependent anisotropic yield criterion, International Journal of Plasticity 38 (2012) 14–26.

[37] A. S. Khan, H. Liu, Strain rate and temperature dependent fracture criteria for isotropic and anisotropic metals, International Journal of Plasticity 37 (2012) 1–15.

[38] A. Y. Ku, A. S. Khan, T. Gnupel-Herold, Quasi-static and dynamic response, and texture evolution of two overaged al 7056 alloy plates in t761 and t721 tempers: Experiments and modeling, International Journal of Plasticity 130 (2020) 102679.

[39] Z. Qian, H. C. Wu, A 2-d texture study based on a double-slip model of polycrystal plasticity with analysis of thin-walled tubes under torsion, International journal of solids and structures 33 (28) (1996) 4167–4193.

[40] M. E. Nixon, O. Cazacu, R. A. Lebensohn, Anisotropic response of high-purity -titanium: Experimental characterization and constitutive modeling, International Journal of Plasticity 26 (4) (2010) 516–532.

[41] R. Krieg, S. Key, Accurate representation of large strain non-proportional plastic flow in ductile materials, Tech. rep., Sandia National Labs., Albuquerque, NM (USA); RE/SPEC, Inc., Albuquerque, NM (USA) (1984).

[42] M. Miller, E. Harley, D. Bammann, Reverse yield experiments and internal variable evolution in polycrystalline metals, International Journal of Plasticity 15 (1) (1999) 93–117.

[43] M. François, A plasticity model with yield surface distortion for non proportional loading, International Journal of Plasticity 17 (5) (2001) 703–717.

[44] A. Shutov, J. Ihlemann, A viscoplasticity model with an enhanced control of the yield surface distortion, International Journal of Plasticity 39 (2012) 152–167.

[45] D. Bammann, M. Chiesa, G. Johnson, Modeling large deformation and failure in manufacturing processes, Theoretical and Applied Mechanics (9) (1996) 359–376.

[46] J. Chaboche, A review of some plasticity and viscoplasticity constitutive theories, International Journal of Plasticity 24 (10) (2008) 1642–1693.

[47] H. P. Feigenbaum, Y. F. Dafalias, Simple model for directional distortional hardening in metal plasticity within thermodynamics, Journal of Engineering Mechanics 134 (9) (2008) 730–738.

[48] H. P. Feigenbaum, Y. F. Dafalias, Directional distortional hardening at large plastic deformations, International Journal of Solids and Structures 51 (23) (2014) 3904–3918.

[49] E. Marin, D. Bammann, R. Regueiro, G. Johnson, On the formulation, parameter identification and numerical integration of the emmi model: Plasticity and isotropic damage, Sandia National Laboratories, Livermore, CA, Report No. SAND2006-0200.

[50] E. Lee, D. Liu, Finite-strain elastic-plastic theory with application to plane-wave analysis, Journal of Applied Physics 38 (1) (1967) 19–27.

[51] E. H. Lee, Elastic-plastic deformation at finite strains, ASME, 1969.

[52] B. D. Coleman, W. Noll, The thermodynamics of elastic materials with heat conduction and viscosity, Archive for Rational Mechanics and Analysis 13 (1) (1963) 167–178.

[53] B. D. Coleman, M. E. Gurtin, Thermodynamics with internal state variables, The Journal of Chemical Physics 47 (2) (1967) 597–613.

[54] U. Kocks, H. Mecking, A mechanism for static and dynamic recovery, Strength of Metals and Alloys (1980) 345–350.

[55] Y. Estrin, H. Mecking, A unified phenomenological description of work hardening and creep based on one-parameter models, Acta Metallurgica 32 (1) (1984) 57–70.

[56] E. Nes, Recovery revisited, Acta metallurgica et materialia 43 (6) (1995) 2189–2207.

[57] S. G. Advani, C. L. Tucker III, The use of tensors to describe and predict fiber orientation in short fiber composites, Journal of Rheology 31 (8) (1987) 751–784.

[58] S. G. Advani, C. L. Tucker III, Closure approximations for three-dimensional structure tensors, Journal of Rheology 34 (3) (1990) 367–386.

[59] V. Lubarda, D. Krajcinovic, Some fundamental issues in rate theory of damage-elastoplasticity, International Journal of Plasticity 11 (7) (1995) 763–797.

[60] D. Bammann, E. Aifantis, A model for finite-deformation plasticity, Acta Mechanica 69 (1-4) (1987) 97–117.

[61] Y. Dafalias, A missing link in the formulation and numerical implementation of finite transformation elastoplasticity, Constitutive equations: Macro and computational aspects (1984) 25–40.

[62] B. Loret, On the effects of plastic rotation in the finite deformation of anisotropic elastoplastic materials, Mechanics of Materials 2 (4) (1983) 287–304.

[63] J. E. Hockett, On relating the flow stress of aluminum to strain, strain rate, and temperature., Tech. rep., Los Alamos Scientific Lab., N. Mex. (1966).

[64] A. Adetokunbo, Enhancing Verification and Validation in Plasticity Using Material Point Simulators, Github:https://github.com/tokshgithub/Multidimentional-Material-Point-Simulator-for-BCJ-and-EMMI.git, 2009.

[65] A. A. Adedoyin, A continuum mechanics approach to modeling and simulating engineering materials undergoing phase transformation using the evolving microstructural model of inelasticity, Mississippi State University, 2014.

[66] Hibbett, Karlsson, Sorensen, ABAQUS/standard: User's Manual, Vol. 1, Hibbitt, Karlsson & Sorensen, 1998.

[67] K. Ken-Ichi, Distribution of directional data and fabric tensors, International Journal of Engineering Science 22 (2) (1984) 149–164.

Appendix A. Incorporating anisotropy plasticity due to texture: generalities

The goal here is to derive and incorporate the anisotropic plasticity due to texture in the EMMI model. Two important parameters for the plasticity model are derived in this appendix: the plastic rate of deformation $\mathbf{d}_p$ and the plastic spin $\mathbf{w}^p$.

It is assumed that the orientation of grains in aggregates are represented by a continuous function representing the crystal orientation as orientation distribution functions (ODF). In general the estimation of the distribution is first determined by achieving a model or parametric form function that describes the orientation distribution. Assuming that $\Gamma(\omega)$ is the given distribution density depending upon the unit vector ω. We want to approximate the distribution density by $F(\omega)$ which involves indeterminated parameters. In this study, ODF functions are represented by an infinite series in polynomial form shown below:

$$F(\omega) = a + a_i\omega_i + a_{ij}\omega_i\omega_j + a_{ijkl}\omega_i\omega_j\omega_k\omega_l + \cdots . \tag{A.1}$$

We also need a criterion to estimate the ODF parameters. The typical approximation is to minimize the least square approximation as

$$\int [F(\omega) - \Gamma(\omega)]^2 \, d\omega \;\longrightarrow\; Min \tag{A.2}$$

The ODF satisfies the conservative equation thanks to the fact that the number of crystals in any initial interval of orientation does not change. Taking inspiration from the previous work by Advani and Tucker [57, 58], we assume that the ODF has the periodicity property which indicates that

$$F(\omega) = F(-\omega). \tag{A.3}$$

Eq.(A.3) can be normalized by

$$\oint \mathrm{d}S = \int_0^{2\pi}\int_0^{\pi} \sin(\theta)\mathrm{d}\theta\mathrm{d}\phi = 4\pi\,, \oint F(\omega)\mathrm{d}\omega = 1. \tag{A.4}$$

Prantil [20] showed that the ODF satisfies the continuity equation

$$\dot{F}(\omega) + F(\omega)\nabla\cdot\dot{\omega} = 0. \tag{A.5}$$

The parameters in Eq.(A.1) known as fabric tensor of third kind proposed by Kanatani [67] can be derived from the equation

$$a_{i_1,i_2,i_3,\ldots,i_n} = \oint \Gamma\left(\omega\right)\left\{\omega_{i_1}\omega_{i_2}\omega_{i_3}\cdots\omega_{i_n}\right\}\mathrm{d}\omega, \tag{A.6}$$

where $\left\{\omega_{i_1}\omega_{i_2}\omega_{i_3}\cdots\omega_{i_n}\right\}$ is the deviatoric part of $\omega_{i_1}\omega_{i_2}\omega_{i_3}\cdots\omega_{i_n}$ tensor. Using the first two terms and by truncating the higher order terms, the ODF yields the expression

$$F\left(\omega\right) = \frac{1}{2\pi} + \frac{2}{\pi}a_{ij}f_{ij}\left(\omega\right) \tag{A.7}$$

where

$$\begin{aligned} f_{ij}(\omega) &= \omega_i \omega_j - \frac{1}{3}\delta_{ij} \\ a_{ij} &= \oint \Gamma(\omega) f_{ij}(\omega)\,\mathrm{d}\omega. \end{aligned} \tag{A.8}$$

In Eq.(A.8) a_{ij} is the structure tensor componenent. Therefore, the orientation of actual experimental data represented by $\Gamma(\omega)$ helps to identify a second rank tensor. Then, the statistical distribution of the orientation can be represented by Eq.(A.7).

While the stress varies during the deformation process in materials, the crystal structure may orient in different directions. The reorientation of the crystal indicates that the tensorial constant a_{ij} in the ODF should vary in order to carry out the information of the orientation of the crystal in aggregate. For this we intend to formulate an evolution equation for the structure tensor to be able to carry the anisotropic texture information during deformation process.

The continuity equation Eq.(A.5) indicates that the grain orientation update $\dot{\omega}$ should be determined. The plastic spin $\mathbf{w}_p$ is the main cause of the grain reorientation. Then, from Prantil [20] the grain orientation update equation can be written as

$$\dot{\omega} = \mathbf{w}_p \omega \tag{A.9}$$

It follows that, the Jaummann derivative of the grain orientation is given by

$$\tilde{\omega} = \dot{\omega} - \mathbf{w}\omega = \lambda_g \mathbf{d}_p \omega - \lambda_g (\omega \cdot \mathbf{d}_p \omega)\,\omega \tag{A.10}$$

Substituting the above Eq.(A.10) into the continuity equation Eq.(A.5) gives

$$\nabla \cdot \tilde{\omega} = \nabla \cdot (\lambda_g \mathbf{d}_p \omega - \lambda_g (\omega \cdot \mathbf{d}_p \omega)\,\omega) = -2\lambda_g (\omega \cdot \mathbf{d}_p \omega) \tag{A.11}$$

with

$$\dot{F}(\omega) = F(\omega)\,(2\lambda_g \omega \cdot \mathbf{d}_p \omega)\,. \tag{A.12}$$

The material time derivative of the structure tensor definition is

$$\dot{a}_{ij} = \overline{\oint F(\omega)\, f_{ij}(\omega)\, d\omega}^{\,\cdot} = \oint \dot{F}(\omega)\, f_{ij}(\omega)\, d\omega + \oint F(\omega)\, \dot{f}_{ij}(\omega)\, d\omega. \tag{A.13}$$

From the grain orientation update equation Eq.(A.11) we get

$$\begin{aligned} \dot{f}_{ij} &= \dot{\omega} \otimes \omega + \omega \otimes \dot{\omega} \\ &= \lambda_g \left((\omega \otimes \omega - \mathbf{I})\,\mathbf{d}_p \omega\right) \otimes \omega + \lambda_g \omega \left((\omega \otimes \omega - \mathbf{I})\,\mathbf{d}_p \omega\right) \\ &= \lambda_g \left(\mathbf{d}_p \omega \otimes \omega + \omega \otimes \mathbf{d}_p \omega - 2\,(\omega \cdot \mathbf{d}_p \omega)\,(\omega \otimes \omega)\right) \end{aligned} \tag{A.14}$$

and the equation Eq.(A.15) expands as follows:

$$
\begin{aligned}
\dot{a}_{ij} &= \overline{\oint F(\omega)\, f_{ij}(\omega)\, d\omega}^{\,\cdot} = \oint \dot{F}(\omega)\, f_{ij}(\omega)\, d\omega + \oint F(\omega)\, \dot{f}_{ij}(\omega)\, d\omega \\
&= \oint F(\omega)\left(2\lambda_g\left(\omega\cdot\mathbf{d}_p\omega\right)\right) f_{ij}(\omega)\, d\omega \\
&+ \oint \dot{F}(\omega)\, \lambda_g\left(\mathbf{d}_p\omega\otimes\omega + \omega\otimes\mathbf{d}_p\omega - 2\left(\omega\mathbf{d}_p\omega\right)\left(\omega\otimes\omega\right)\right) d\omega \\
&= 2\lambda_g\left(\omega\cdot\mathbf{d}^p\omega\right)\oint F(\omega)\, f_{ij}(\omega)\, d\omega \\
&+ \lambda_g\oint F(\omega)\left(\mathbf{d}_p\omega\otimes\omega + \omega\otimes\mathbf{d}_p\omega - 2\left(\omega\cdot\mathbf{d}_p\omega\right)\left(\omega\otimes\omega\right)\right) d\omega \\
&= 2\lambda_g\left(\omega\cdot\mathbf{d}_p\omega\right) a_{ij} + \lambda_g\oint F(\omega)\left(\mathbf{d}_p\omega\otimes\omega + \omega\otimes\mathbf{d}_p\omega\right) d\omega \\
&- 2\lambda_g\left(\omega\cdot\mathbf{d}_p\omega\right)\oint F(\omega)\left(\omega\otimes\omega - \frac{1}{3}\delta_{ij} + \frac{1}{3}\delta_{ij}\right) d\omega \\
&= -2\lambda_g\left(\omega\cdot\mathbf{d}_p\omega\right) a_{ij} + \lambda_g\left(\mathbf{a}\mathbf{d}_p + \mathbf{d}_p\mathbf{a} + \frac{2}{3}\mathbf{d}_p\right) \\
&+ \frac{2}{3}\lambda_g\left(\omega\cdot\mathbf{d}_p\omega\right)\oint F(\omega)\,\delta_{ij} d\omega
\end{aligned}
\tag{A.15}
$$

with

$$
\dot{\mathbf{a}} = \lambda_g\left(\mathbf{a}\mathbf{d}_p + \mathbf{d}_p\mathbf{a} + \frac{2}{3}\mathbf{d}_p\right) - 2\lambda_g\mathbf{B} : \mathbf{d}_p + \frac{2}{3}\lambda_g\left(\omega\cdot\mathbf{d}_p\omega\right)\mathbf{I} \tag{A.16}
$$

Based on the multiplicative decomposition of the deformation gradient into elastic and plastic parts $\mathbf{F} = \mathbf{F}^e\mathbf{F}^p$ the evolution equation for the structure tensor $\mathbf{a}$ in the intermediate configuration is

$$
\tilde{\mathbf{a}} = \mathbf{F}^p\left(\overline{\mathbf{F}^{p^{-1}}\mathbf{a}\mathbf{F}^p}^{\,\cdot}\right)\mathbf{F}^{p^{-1}} = \dot{\mathbf{a}} - \mathbf{l}_p\mathbf{a} + \mathbf{a}\mathbf{l}_p. \tag{A.17}
$$

Combining Eqs.(A.15) and (A.17) the evolution equation for the structure tensor $\mathbf{a}$ becomes

$$
\begin{aligned}
\tilde{\mathbf{a}} &= \dot{\mathbf{a}} - \mathbf{w}_p\mathbf{a} + \mathbf{a}\mathbf{w}_p \\
&= \mathbf{a}\mathbf{w}_p - \mathbf{w}_p\mathbf{a} + \lambda_g\left(\mathbf{a}\mathbf{d}_p + \mathbf{d}_p\mathbf{a} + \frac{2}{3}\mathbf{d}_p\right) \\
&+ \frac{2}{3}\lambda_g\left(\omega\cdot\mathbf{d}_p\omega\right)\mathbf{I} - 2\lambda_g\mathbf{B} : \mathbf{d}_p
\end{aligned}
\tag{A.18}
$$

where $\mathbf{B}$ is a fourth rank tensor defined as

$$
B_{ijkl} = \oint F(\omega)\omega_i\omega_j\omega_k\omega_l d\omega. \tag{A.19}
$$

Appendix B. Closure approximation

The structure tensor a_{ij} is the moment of the distribution function $F(\omega)$, and its evolution equation of **a** represents a closure problem. The evolution equation Eq.(A.18) for any tensor always contains the next higher even-order tensor (Advani and Tucker [57, 58]). Therefore, the evolution equation of second order structure tensor contains a fourth order tensor B_{ijkl}. It is required to develop some approximation to obtain a close set of evolution equations. The closure approximation should contain several assumptions including

1. the approximation must only be from the lower order orientation tensors and the unit tensor;
2. the approximation must satisfy normalization conditions in the equations as below

$$a_{ii} = 1,\ B_{ijkk} = a_{ij}; \tag{B.1}$$

3. the approximation should maintain the symmetry of orientation tensor:

$$\left\{ \begin{array}{l} a_{ij} = a_{ji} \\ B_{ijkl} = B_{jikl} = B_{kijl} = B_{lijk} = B_{klij}. \end{array} \right. \tag{B.2}$$

In the susequent we use a linear closure approximation for the fourth order tensor B_{ijkl} using all of the products of a_{ij} and δ_{ij}.

For three-dimensional orientation the linear approximation of fourth order tensor becomes

$$\begin{aligned} \hat{B}_{ijkl} = {} & \frac{1}{7}\left(a_{ij}\delta_{kl} + a_{ik}\delta_{jl} + a_{il}\delta_{jk} + a_{kl}\delta_{ij} + a_{jl}\delta_{ik} + a_{jk}\delta_{il}\right) \\ & - \frac{1}{35}\left(\delta_{ij}\delta_{kl} + \delta_{ik}\delta_{jl} + \delta_{il}\delta_{jk}\right) \end{aligned} \tag{B.3}$$

Another way to form a closure approximation is to omit the linear terms and take the product of lower order tensors. This is known as quadratic closure, $\widetilde{B}_{ijkl}$, which is defined as

$$\widetilde{B}_{ijkl} = a_{ij}a_{kl} \tag{B.4}$$

The quadratic closure does not have all the symmetry properties of the components B_{ijkl} but it has the symmetry properties of elasticity tensor and presents no difficulty for mechanical property predictions. It is worth mentioning that once this approximation is used in the evolution equation, it preserves the symmetry of the tensor a_{ij}. In dilute short fiber composites, it is shown that the linear closure approximations are exact for a completely random distribution of fiber orientation while the quadratic closure approximations are exact for perfect uniaxial alignments of the fibers. Hence, the combination of the two closure approximations can offer the orientation information for the entire range of orientations.

A hybrid closure approximation $\bar{B}_{ijkl}$ is constructed by combining the two presented approximations as

$$\bar{B}_{ijkl} = (1-f)\,\hat{B}_{ijkl} + \widetilde{B}_{ijkl} \tag{B.5}$$

where f is a generalization of Herman's orientation factor; it is equal to zero for randomly oriented inclusions and unity for perfectly aligned inclusions. The scalar measure f is defined as

$$f = C_1 a_{ij} a_{ji} - C_2 = \frac{3}{2} a_{ij} a_{ji} - \frac{1}{2} \tag{B.6}$$

for three dimensional orientation which is an invariant of the structure tensor **a**. Applying the closure approximation to the last term in Eq.(A.18) we get

$$\begin{aligned} b_{ijkl} d_{p,kl} = (1-f) &\left(-\frac{1}{35} \left(2\mathbf{d}_p \right) + \frac{1}{7} \left(\mathbf{a}\mathbf{d}_p + \mathbf{a}\mathbf{d}_p + \left(\mathbf{a} : \mathbf{d}_p \right) \delta_{ij} + \mathbf{a}\mathbf{d}_p + \mathbf{d}_p \mathbf{a} \right) \right) \\ &+ f \left(\mathbf{a} : \mathbf{d}_p \right) a_{ij} \end{aligned}$$

or in a compact form:

$$\begin{aligned} \mathbf{B} : \mathbf{d}_p = (1-f) &\left(-\frac{1}{35} \left(2\mathbf{d}_p \right) + \frac{1}{7} \left(2\mathbf{a}\mathbf{d}_p + \left(\mathbf{a} : \mathbf{d}_p \right) \mathbf{I} + 2\mathbf{d}_p \mathbf{a} \right) \right) \\ &+ f \left(\mathbf{a} : \mathbf{d}_p \right) \mathbf{a} \end{aligned} \tag{B.7}$$

Hence, the final evolution equation of the structure tensor reads:

$$\begin{aligned} \tilde{\mathbf{a}} &= \dot{\mathbf{a}} - \mathbf{w}_p \mathbf{a} + \mathbf{a} \mathbf{w}_p \\ &= -2\lambda_g (1-f) \left(-\frac{1}{35} \left(2\mathbf{d}_p \right) + \frac{1}{7} \left(2\mathbf{a}\mathbf{d}_p + \left(\mathbf{a} : \mathbf{d}_p \right) \delta_{ij} + 2\mathbf{a}\mathbf{d}_p \right) \right) \\ &- 2\lambda_g f \left(\mathbf{a} : \mathbf{d}_p \right) \mathbf{a} + \lambda_g \left(\mathbf{a}\mathbf{d}_p + \mathbf{d}_p \mathbf{a} + \frac{2}{3} \mathbf{d}_p \right) + \frac{2}{3} \lambda_g \left(\mathbf{a} : \mathbf{d}_p \right) \mathbf{I} - \mathbf{w}_p \mathbf{a} + \mathbf{a} \mathbf{w}_p \end{aligned} \tag{B.8}$$

with the equation

$$\left(\mathbf{a} : \mathbf{d}_p \right) = \omega \cdot \mathbf{d}_p \omega \tag{B.9}$$

where λ_g is a geometric parameter dependent on slip system orientation. The plastic spin of the aggregate in the intermediate configuration is defined by averaging the plastic spin in each grain using ODF as

$$\mathbf{w}_p = \oint \mathbf{a}\,(\omega)\, \mathbf{w}_g^p(\omega) d\omega = \lambda_g \left(\mathbf{a}\mathbf{d}_p - \mathbf{d}_p \mathbf{a} \right).$$

The asymmetric part of the velocity gradient should be added to the skew-symmetric part to obtain the velocity gradient in the deformation process

$$\mathbf{l}_p = \mathbf{d}_p + \mathbf{w}_p \tag{B.10}$$

The symmetric part of velocity gradient $\mathbf{d}_p$ is defined separately by its magnitude $||\mathbf{d}_p||$ and its direction **N**:

$$\mathbf{d}_p = ||\mathbf{d}_p||\mathbf{N} \tag{B.11}$$

The magnitude of the symmetric part of the velocity gradient which is called the evolution of plastic flow is written in the unified creep plasticity form as

$$||\mathbf{d}_p|| = \sqrt{\frac{2}{3}} f\left(\theta\right)\left(\sinh\left(\Phi\right)\right)^{n(\theta)} \tag{B.12}$$

where the function $f(\theta)$ determines the strain rate at which the model transitions from rate-independent to rate-dependent behavior, $n(\theta)$ is the temperature dependent rate sensitivity parameter and, the term inside the hyperbolic sine function called the plastic potential Φ function is defined by the relation

$$\Phi = \left[\frac{\sigma_{eq}}{\bar{\chi}\bar{\kappa} + \mathrm{Y}_0} - 1\right] \tag{B.13}$$

where σ_{eq} the magnitude of a second rank tensor including the deviatoric part of the Piola-Kirchhoff stress; the back stress is defined as

$$\sigma_{eq} = \sqrt{\frac{2}{3}}||\boldsymbol{\xi}|| \tag{B.14}$$

with

$$\boldsymbol{\xi} = \boldsymbol{\sigma}' - \frac{2}{3}\boldsymbol{\alpha}. \tag{B.15}$$

Two terms in the denominator of Eq.(B.13) are $\bar{\kappa}$ and $\bar{\chi}$ which are related to the dislocation density and the directional distortion.

The directional distortion is defined based on the cosine series as

$$\bar{\chi} = 1 + a_1\cos(\bar{\eta}) + a_2\cos 2(\bar{\eta}) + a_3\cos 3(\bar{\eta}) + a_4\cos 4(\bar{\eta}). \tag{B.16}$$

The angles in the cosine series are calculated from the angle between the stress tensor $\boldsymbol{\xi}$ and the structure tensor **a**:

$$\cos(\bar{\eta}) = \cos(\bar{\eta}) = \frac{\boldsymbol{\xi} : \mathbf{a}}{||\boldsymbol{\xi}||||\mathbf{a}||} \tag{B.17}$$

Since there is no flow surface defined for this model, the plastic potential function Φ is used to define the direction of the plastic flow. The direction of plastic flow $\mathbf{N}^p$ derived as

$$\mathbf{N} = sym\left(\frac{\partial\bar{\Phi}}{\partial\boldsymbol{\xi}}\right)\Big/||sym\left(\frac{\partial\Phi}{\partial\boldsymbol{\xi}}\right)|| \tag{B.18}$$

with

$$\begin{aligned}\frac{\partial\Phi}{\partial\boldsymbol{\xi}} &= \partial\left[\frac{\sigma_{eq}}{\bar{\chi}\bar{\kappa}+\mathrm{Y}_0}-1\right]\Big/\left(\frac{\partial\sigma_{eq}}{\partial\boldsymbol{\xi}}\bar{\chi}\bar{\kappa}-\bar{\kappa}\frac{\partial\bar{\chi}}{\partial\boldsymbol{\xi}}\sigma_{eq}\right)\Big/\left(\bar{\chi}\bar{\kappa}\right)^2 \\ &= \frac{1}{\bar{\chi}\bar{\kappa}}\left(\frac{\partial\sigma_{eq}}{\partial\boldsymbol{\xi}}-\frac{\sigma_{eq}}{\bar{\chi}}\frac{\partial\bar{\chi}}{\partial\boldsymbol{\xi}}\right)\end{aligned}\tag{B.19}$$

where $\bar{\chi}$ and $\bar{\kappa}$ are scalars which are related toward the equation

$$\begin{aligned}\mathbf{N} &= sym\left(\frac{\partial\Phi}{\partial\boldsymbol{\xi}}\right)\Big/||sym\left(\frac{\partial\Phi}{\partial\boldsymbol{\xi}}\right)|| \\ &= \frac{1}{\bar{\chi}\bar{\kappa}}sym\left(\frac{\partial\sigma_{eq}}{\partial\boldsymbol{\xi}}-\frac{\sigma_{eq}}{\bar{\chi}}\frac{\partial\bar{\chi}}{\partial\boldsymbol{\xi}}\right)\Big/||sym\left(\frac{\partial\sigma_{eq}}{\partial\boldsymbol{\xi}}-\frac{\sigma_{eq}}{\bar{\chi}}\frac{\partial\bar{\chi}}{\partial\boldsymbol{\xi}}\right)||\end{aligned}\tag{B.20}$$

with

$$\frac{\partial\sigma_{eq}}{\partial\boldsymbol{\xi}} = \sqrt{\frac{3}{2}}\frac{\boldsymbol{\xi}}{||\boldsymbol{\xi}||}$$

and

$$\begin{aligned}\frac{\partial\bar{\chi}}{\partial\boldsymbol{\xi}} &= \frac{\partial\bar{\chi}}{\partial\cos(\bar{\eta})}\frac{\partial\cos(\bar{\eta})}{\partial\boldsymbol{\xi}} = \frac{\partial\bar{\chi}}{\partial\cos(\bar{\eta})}\partial\left(\frac{\boldsymbol{\xi}:\mathbf{a}}{||\boldsymbol{\xi}||||\mathbf{a}||}\right)\Big/\partial\boldsymbol{\xi} \\ &= \frac{\partial\bar{\chi}}{\partial\cos(\bar{\eta})}\left(\frac{\partial\left(\boldsymbol{\xi}:\mathbf{a}\right)}{\partial\boldsymbol{\xi}}||\boldsymbol{\xi}||||\mathbf{a}||-\frac{\partial\left(||\boldsymbol{\xi}||||\mathbf{a}||\right)}{\partial\boldsymbol{\xi}}\left(\boldsymbol{\xi}:\mathbf{a}\right)\right)\Big/||\boldsymbol{\xi}||^2||\mathbf{a}||^2 \\ &= \frac{1}{||\boldsymbol{\xi}||||\mathbf{a}||}\frac{\partial\bar{\chi}}{\partial\cos(\bar{\eta})}\left[\frac{\partial\left(\boldsymbol{\xi}:\mathbf{a}\right)}{\partial\boldsymbol{\xi}}-\frac{\partial\left(||\boldsymbol{\xi}||||\mathbf{a}||\right)}{\partial\boldsymbol{\xi}}\frac{\left(\boldsymbol{\xi}:\mathbf{a}\right)}{||\boldsymbol{\xi}||||\mathbf{a}||}\right] \\ &= \frac{1}{||\boldsymbol{\xi}||||\mathbf{a}||}\frac{\partial\bar{\chi}}{\partial\cos(\bar{\eta})}\left[\mathbf{a}-\frac{\partial\left(||\boldsymbol{\xi}||||\mathbf{a}||\right)}{\partial\boldsymbol{\xi}}\frac{\left(\boldsymbol{\xi}:\mathbf{a}\right)}{||\boldsymbol{\xi}||||\mathbf{a}||}\right] \\ &= \frac{1}{||\boldsymbol{\xi}||||\mathbf{a}||}\frac{\partial\bar{\chi}}{\partial\cos(\bar{\eta})}\left[\mathbf{a}-\frac{\boldsymbol{\xi}}{||\boldsymbol{\xi}||}\frac{\left(\boldsymbol{\xi}:\mathbf{a}\right)}{||\boldsymbol{\xi}||}\right] \\ &= \frac{1}{||\boldsymbol{\xi}||||\mathbf{a}||}\frac{\partial\bar{\chi}}{\partial\cos(\bar{\eta})}\left[\mathbf{a}-\left(\frac{\left(\boldsymbol{\xi}:\mathbf{a}\right)}{\left(\boldsymbol{\xi}:\boldsymbol{\xi}\right)}\right)\boldsymbol{\xi}\right] \\ &= \frac{a_1+4a_2\cos(\bar{\eta})+3a_3\left(4\cos^2(\bar{\eta})-1\right)+16a_4\cos(\bar{\eta})\left(4\cos^2(\bar{\eta})-1\right)}{||\boldsymbol{\xi}||||\mathbf{a}||} \\ &\times\left[\mathbf{a}-\left(\frac{\left(\boldsymbol{\xi}:\mathbf{a}\right)}{\left(\boldsymbol{\xi}:\boldsymbol{\xi}\right)}\right)\boldsymbol{\xi}\right]\end{aligned}\tag{B.21}$$

where the following relations

$$\frac{\partial\bar{\chi}}{\partial\cos(\bar{\eta})} = a_1+4a_2\cos(\bar{\eta})+3a_3\left(4\cos^2(\bar{\eta})-1\right)+16a_4\cos(\bar{\eta})\left(4\cos^2(\bar{\eta})-1\right),$$

$$\frac{\partial\left(||\boldsymbol{\xi}||||\mathbf{a}||\right)}{\partial\boldsymbol{\xi}} = \frac{\partial\left(||\boldsymbol{\xi}||\right)}{\partial\boldsymbol{\xi}}||\mathbf{a}|| = \frac{\boldsymbol{\xi}}{||\boldsymbol{\xi}||}||\mathbf{a}||,$$

$$||\boldsymbol{\xi}||^2 = \boldsymbol{\xi} : \boldsymbol{\xi}$$

and

$$\frac{\partial\left(\boldsymbol{\xi} : \mathbf{a}\right)}{\partial \boldsymbol{\xi}} = \mathbf{a}$$

hold.